

Cite this article as: Bi Guangli, Wei Zhichao, Jiang Jing, et al. Effects of Co-addition of Ni and Zn on Microstructure and Mechanical Properties of Extruded Mg-Y-Cu Alloy[J]. Rare Metal Materials and Engineering, 2025, 54(05): 1145-1155. DOI: <https://doi.org/10.12442/j.issn.1002-185X.20240205>.

ARTICLE

# Effects of Co-addition of Ni and Zn on Microstructure and Mechanical Properties of Extruded Mg-Y-Cu Alloy

Bi Guangli<sup>1,2</sup>, Wei Zhichao<sup>1,2</sup>, Jiang Jing<sup>1,2</sup>, Zhang Niuming<sup>3</sup>, Li Yuandong<sup>1,2</sup>, Chen Tijun<sup>1,2</sup>

<sup>1</sup> State Key Laboratory of Advanced Processing and Recycling of Nonferrous Metals, Lanzhou University of Technology, Lanzhou 730050, China; <sup>2</sup> School of Materials Science and Engineering, Lanzhou University of Technology, Lanzhou 730050, China; <sup>3</sup> Guizhou Fenghua Aerospace Precision Equipment Co., Ltd, Guiyang 550000, China

**Abstract:** The effects of the co-addition of Ni and Zn on the microstructure and mechanical properties of the extruded Mg-6.84Y-2.45Cu (MYC, wt%) alloy were researched. Results show that the as-cast Mg-6.79Y-1.21Cu-1.12Ni-1.25Zn (MYCNZ, wt%) alloy consists of the  $\alpha$ -Mg, a few Y-rich phases, lamellar 18R-long period stacking ordered (LPSO) phase, and granular Mg<sub>2</sub>(Cu, Ni, Zn) phase. After the homogenization process, phase transformation occurs in MYCNZ alloy. Some 18R-LPSO phases at the grain boundary are transformed into the thin striped 14H-LPSO phase in the grains. After extrusion, the amount, morphology, and distribution of the second phase are changed, and the grain size of the extruded MYCNZ alloy is significantly reduced to approximately 2.62  $\mu\text{m}$ . Additionally, a weaker basal texture is formed in the extruded MYCNZ alloy. The tensile results indicate that the co-addition of Ni and Zn significantly enhances the tensile strength of the extruded MYC alloy while maintaining good ductility. The tensile yield strength ( $\sigma_{0.2}$ ), ultimate tensile strength ( $\sigma_b$ ), and elongation to failure ( $\epsilon_f$ ) of the extruded MYCNZ alloy are 266.9 MPa, 299.8 MPa, and 20.1%, respectively. This alloy has a good strength-plastic synergistic effect. The excellent tensile strength of the extruded MYCNZ alloy at room temperature is mainly due to grain refinement and the second phase strengthening effect, and its outstanding ductility is ascribed to the texture weakening and activation of non-basal slips.

**Key words:** extruded Mg-Y-Cu(Ni, Zn) alloy; LPSO phase; microstructure; mechanical properties

## 1 Introduction

Magnesium (Mg) alloys have gained significant attention owing to their low density, high specific strength, and commendable heat resistance<sup>[1-3]</sup>. However, in comparison to aluminum (Al) alloys and steel, the inferior tensile strengths and inadequate room-temperature ductility of these alloys significantly impede their development and utilization. Currently, the wrought Mg-rare earth (RE)-transition metal (TM) alloys with a long period stacking ordered (LPSO) phase have demonstrated excellent mechanical properties at room temperature (RT)<sup>[4-5]</sup>.

In addition to grain boundary strengthening and texture strengthening, the high mechanical properties of the Mg-RE-

TM alloys are mainly attributed to the precipitation strengthening, similar fiber reinforcement in composite materials, and kink strengthening resulting from LPSO phase<sup>[6-8]</sup>. It is noteworthy that these three types of strengthening mechanisms are directly influenced by the properties of LPSO phase, such as morphology, number, size, and structure<sup>[9-10]</sup>. Therefore, altering the properties of LPSO phase through alloying, heat treatment, and hot processing, including rolling, extrusion, and forging, is an effective method to improve the mechanical properties of Mg-RE-TM alloys<sup>[11]</sup>. For example, the addition of Zn into Mg-Y(Co) alloys can significantly decrease the critical resolved shear stress (CRSS) for both basal and non-basal slip systems, thereby facilitating the activation of non-basal slips and

Received date: April 07, 2024

Foundation item: Major Science and Technology Project of Gansu Province (22ZD6GA008); National Natural Science Foundation of China (52261027, 51961021, 52001152); Open Project of State Key Laboratory for Mechanical Behavior of Materials (20192102); Undergraduate Innovation and Entrepreneurship Training Program (DC20231188, DC20231482, DC20231558, DC20231469, DC20231441); Supported by Sinoma Institute of Materials Research (Guang Zhou) Co., Ltd (SIMR)

Corresponding author: Bi Guangli, Ph. D., Professor, State Key Laboratory of Advanced Processing and Recycling of Nonferrous Metals, Lanzhou University of Technology, Lanzhou 730050, P. R. China, Tel: 0086-931-2976378, E-mail: glbi@163.com

Copyright © 2025, Northwest Institute for Nonferrous Metal Research. Published by Science Press. All rights reserved.

improving the ductility of the alloys<sup>[12-14]</sup>. Notably, the extruded Mg-1.4Y-0.6Zn-0.2Co (at%) alloy exhibits an excellent elongation to failure ( $\epsilon_L$ ) of 32%, surpassing that of the previously reported Mg-RE series alloys<sup>[14]</sup>. The addition of 3% Ni can facilitate the precipitation of a multitude of LPSO phases and significantly refine the grains of Mg-3Y (at%) alloy, thereby enhancing RT tensile properties. Furthermore, the increase in volume fraction of the bulk LPSO phase, which impedes dislocation movement in both dynamic recrystallization (DRX) and non-DRX grains of the extruded Mg-Y-Ni alloy, contributes to the enhancement in yield strength ( $\sigma_{0.2}$ =502 MPa)<sup>[15]</sup>. Additionally, Zhang et al<sup>[16]</sup> demonstrated that the co-addition of Cu and Ni into the Mg-2Y alloy after homogenization and extrusion could significantly refine LPSO phases and increase their amount, effectively increasing the tensile properties of the Mg<sub>96</sub>Y<sub>2</sub>Cu<sub>1</sub>Ni<sub>1</sub> (at%) alloy. Zhou et al<sup>[17]</sup> confirmed that the alloying of 1.1wt% Zn and 0.5wt% Zr not only refined grains but also promoted the formation of LPSO kink bands in the extruded Mg-5.5Gd-4.4Y (wt%) alloy. The LPSO kink bands not only impeded the dislocation movement but also regulated stress concentration during plastic deformation. The dual effects enhanced the workability and ductility of the extruded Mg-Gd-Y-Zn-Zr alloy. Bi et al<sup>[10]</sup> pointed out that the co-addition of 0.5at% Zn and 0.5at% Ni into Mg-2Y (at%) alloy led to the precipitation of LPSO phase with three kinds of morphologies (blocky, lamellar, and thin striped) and increased the volume fraction of LPSO phase. As a result, the extruded Mg-2Y-0.5Zn-0.5Ni (at%) alloy demonstrated excellent strength and ductility with tensile yield strength ( $\sigma_{0.2}$ ), ultimate tensile strength ( $\sigma_b$ ), and elongation to failure ( $\epsilon_L$ ) of 336 MPa, 389 MPa, and 12.6%, respectively.

As previously mentioned, most studies have focused on the effects of the addition of one or two types of TM elements on the microstructure and mechanical properties of Mg-Y alloys. However, the effects of incorporating three TM elements into Mg-Y alloys are rarely reported. Considering the disparity in the atomic radius and solid solubility of TM elements in the  $\alpha$ -Mg matrix, the addition of multiple TM elements undoubtedly alters the properties of LPSO phases.

Therefore, in this research, the extruded Mg-2Y-0.5Cu-0.5Zn-0.5Ni (at%) alloy was prepared and its microstructure evolution and mechanical properties were examined. The corresponding strengthening and toughening mechanisms were also discussed. The research provided valuable references for the development of high-performance Mg alloys.

## 2 Experiment

The Mg-6.79Y-1.21Cu-1.12Ni-1.25Zn (MYCNZ, wt% ) alloys were fabricated by high-purity Mg (99.99%), Zn (99.99%), and master alloys of Mg-15Cu (wt%), Mg-15Ni (wt%), and Mg-20Y (wt%). Melting process was conducted in a graphite crucible positioned within a pit-type resistance furnace (SG2-7.5-12) at 720 °C under a gas mixture condition of CO<sub>2</sub> and SF<sub>6</sub>. A cylindrical ingot with 90 mm in diameter and 500 mm in length was obtained from a water-cooled mold

and then homogenization was conducted at 400 °C for 12 h. Subsequently, the homogenized ingot was extruded into a sheet (width: 40 mm; thickness: 10 mm) using a 630 t extruder. Besides, the extruded sheet was water-quenched to prevent grain growth of the alloy. The extrusion parameters comprised the temperature of 366 °C, speed of 0.5 m/s, and extrusion ratio of 17:1.

The microstructure of the samples was analyzed using laser confocal optical microscope (OM, LSM 800) and scanning electron microscope (SEM, JEM-2100F) coupled with energy dispersive spectrometer (EDS). The phase structure and composition were characterized by X-ray diffractometer (XRD, Rigaku D/max 2500 PC). The samples for OM and SEM observation were prepared by grinding and mechanical polishing. Subsequently, the samples were subjected to an acid etching process for approximately 15–25 s. The acid solution consisted of 5 g picric acid and 4vol% nitric acid. The electron backscattered diffraction (EBSD) data of the extruded alloy were analyzed, including average grain sizes, pole figure (PF), and inverse pole figure (IPF). EBSD measurements were conducted at steps of 0.2 and 0.4  $\mu\text{m}$  with an operating voltage of 20 kV. All EBSD data were processed and analyzed by Channel 5 software. Furthermore, transmission electron microscope (TEM, FEI Talos F200X) was employed to investigate the phase structure and dislocation distribution of the extruded alloy. High-resolution bright-field TEM (HRTEM) images and selected area electron diffraction (SAED) patterns were obtained simultaneously during TEM observation.

The tensile testing was conducted using a tensile tester (AGS-X 300 kN) with the Y10/5 extensometer at RT at the strain rate of  $1 \times 10^{-3} \text{ s}^{-1}$ . To ensure the data accuracy, three samples of 43 mm $\times$ 8 mm $\times$ 2.5 mm were employed for the tensile tests along the extrusion direction (ED). The engineering stress-engineering strain curves were obtained using Origin software, and the tensile surface morphology of alloys was observed by SEM.

## 3 Results and Discussion

### 3.1 Microstructures

Fig. 1 displays OM and SEM images of the MYCNZ alloy at as-cast, homogenized, and extruded states. Compared with those of the extruded Mg-2Y-0.5Cu (MYC, at%) alloy, the co-addition of Zn and Ni not only refines the grains but also modifies the second phase<sup>[18]</sup>. The as-cast MYCNZ alloy is composed of the  $\alpha$ -Mg matrix, numerous lamellar phases, and a small number of irregular particles, as shown in Fig. 1a and 1d. Based on EDS results, the gray lamellar phases observed at the dendrite grain boundary are confirmed as 18R-LPSO phases, while the particle phases are MgY and Y-rich phases. Additionally, the presence of 18R-LPSO phases in the as-cast alloy is further confirmed by XRD patterns, as shown in Fig. 2. However, the MgY and Y-rich phases are not indexed due to their small amount. It is worth noting that the co-addition of Zn and Ni results in the formation of larger-size square granular phases at the grain boundaries in the as-cast MYCNZ alloy. The diffraction peak of those phase shifts a little bit

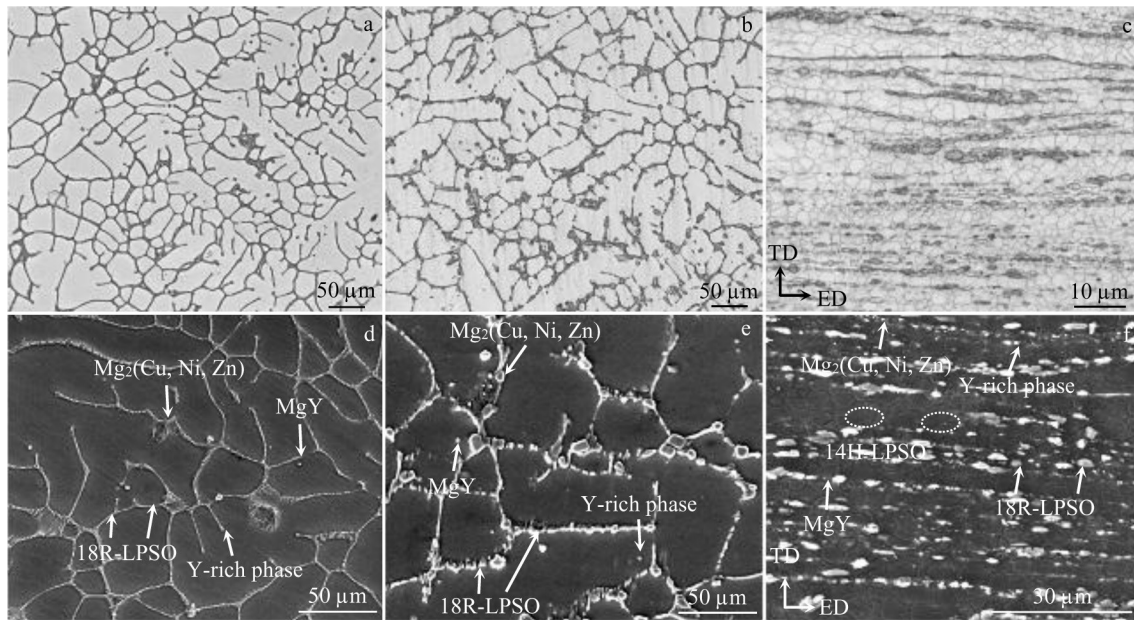


Fig.1 OM (a–c) and SEM (d–f) images of as-cast (a, d), as-homogenized (b, e), and extruded (c, f) MYCNZ alloys

towards the left side, compared with that of the  $Mg_2Cu$  phase in as-cast MYC alloy. Based on the chemical composition of Mg-17.7Cu-11.1Ni-4.6Zn (at%) alloy, the granular phase is identified as  $Mg_2(Cu, Ni, Zn)$  phase.

OM and SEM microstructures of as-homogenized MYCNZ alloy are shown in Fig. 1b and 1e, respectively. After homogenization, some thin striped phases are precipitated in the  $\alpha$ -Mg matrix. In comparison to that of the as-cast alloy, the number of these thin striped phases increases, whereas the amount of the lamellar phases decreases. The thin striped phase is identified as 14H-LPSO phase<sup>[10]</sup>. Therefore, it can be concluded that a phase transition occurs during the homogenization process, wherein parts of the lamellar 18R-LPSO phases at the grain boundary are transformed into thin striped 14H-LPSO phases within the grains. This phenomenon can also be observed in other Mg-RE-TM alloys<sup>[19–20]</sup>. Fig. 1c and 1f show OM and SEM images of the extruded MYCNZ alloy, respectively. During extrusion, the grains in the extruded alloy undergo significant refinement attributed to DRX. In addition, multiple second phases are remarkably broken and primarily distributed along ED with a significant quantity of thin striped LPSO phases precipitated within the  $\alpha$ -Mg matrix. LPSO phases of three morphologies appear in the extruded alloy, containing blocky shape, lamellar shape (distributed along ED), and thin striped shape within the grains. Based on EDS analysis, the thin striped phases are 14H-LPSO phase, whereas the phases with lamellar and blocky morphologies are identified as 18R-LPSO phases. Compared with those of extruded MYC alloy, the co-addition of Ni and Zn only alters the volume fraction and chemical composition of LPSO phase, and its crystalline structure does not change. Firstly, the volume fraction of LPSO phase decreases after the addition of Ni and Zn, which is primarily attributed to the consumption of elements Cu, Ni, and Zn to

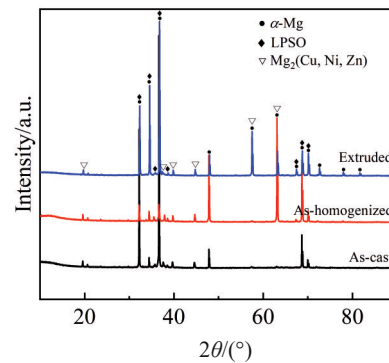


Fig.2 XRD patterns of as-cast, as-homogenized, and extruded MYCNZ alloys

form a large number of  $Mg_2(Cu, Ni, Zn)$  phase in the Mg matrix. Secondly, the chemical composition of the 18R-LPSO phase changes from Mg-4Y-4Cu (at%) in the extruded MYC alloy to Mg-4Y-0.5Cu-1.6Ni-1.9Zn (at%) in the extruded MYCNZ alloy. Similarly, the chemical composition of the 14H-LPSO phase undergoes a transition from Mg-4Y-6Cu (at%) to Mg-4.3Y-1.5Cu-2.2Ni-2.2Zn (at%). The typical square granular phases are precipitated in the Mg matrix of the extruded MYCNZ alloy, and their volume fraction (6.4%) is higher than that of the extruded MYC alloy (4.04%)<sup>[18]</sup>. The increase in the number of these particle phases can enhance the tensile properties of the extruded alloy.

EBSD maps of the extruded MYCNZ alloy are shown in Fig. 3. IPF in Fig. 3a reveals the significant occurrence of DRX in the extruded alloy with an average grain size of approximately 2.62  $\mu m$  (Fig. 3c). As shown in Fig. 3b, the extruded MYCNZ alloy displays a  $\{0001\} \langle 11\bar{2}0 \rangle$  basal texture with a maximum texture intensity of 4.05 with multiple random distributions (MRDs). It is found that the co-

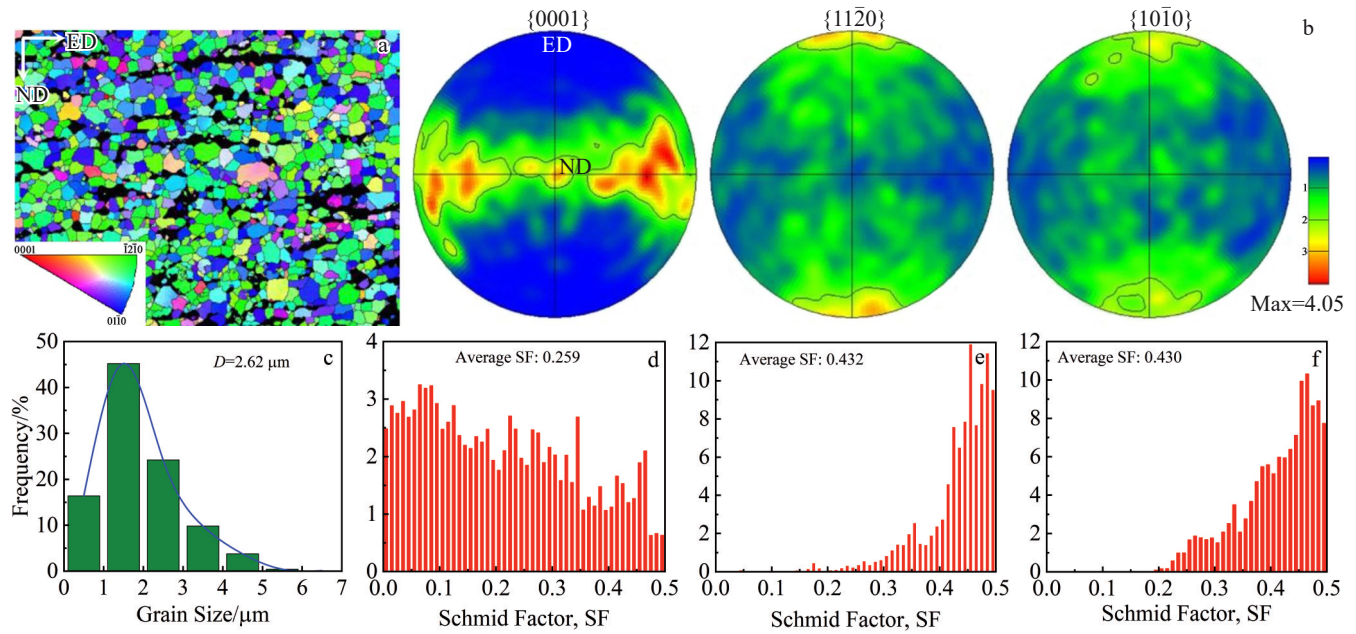


Fig.3 EBSD maps of extruded MYCNZ alloy: (a) IPF and (b) PFs; grain size distribution of extruded MYCNZ alloy (c); Schmid factor distributions of basal slip texture (d), prismatic slip texture (e), and pyramidal slip texture (f) of extruded MYCNZ alloy

addition of Zn and Ni weakens the texture of the extruded alloy, thereby enhancing its ductility<sup>[11]</sup>. Fig.3d–3f show the distribution of Schmid factor (SF) of different slip systems in the extruded MYCNZ alloy. The results reveal that the basal  $\langle a \rangle$  slip in the extruded MYCNZ alloy displays the lowest Schmid factor with an average value of 0.259. According to the Schmid law, slip systems with Schmid factor closer to 0.5 demonstrate higher possibility for activation<sup>[21]</sup>. The average Schmid factor value of the non-basal slip textures is approximately 0.4, which is beneficial to the activation of the non-basal slips and contributes to exceptional ductility in the extruded alloys. CRSS of the slip plane is closely related to the initiation of dislocations<sup>[22]</sup>. In this research, CRSS values of corresponding slip planes are calculated. Nevertheless, the values of strain ( $\varepsilon$ ) and stress ( $\sigma$ ) are related to shear strain ( $\gamma$ ) and critical shear stress ( $\tau$ ) on slip planes in extruded alloys<sup>[23]</sup>. CRSS values for the basal plane ( $\tau_{\text{basal}}$ ), prismatic plane ( $\tau_{\text{prism}}$ ), and pyramidal plane ( $\tau_{\text{pyramidal}}$  or  $\tau_{\langle c+a \rangle}$ ) of the extruded MYC alloy are determined as 49.75, 102.35, and 101.57 MPa, respectively. Those of MYCNZ alloys and 69.13, 129.51, and 128.91 MPa, as shown in Fig. 4a. Therefore, the lower CRSS ratios of  $\tau_{\text{prism}}/\tau_{\text{basal}}$  and  $\tau_{\text{pyramidal}}/\tau_{\text{basal}}$

of two extruded alloys indicate a higher probability of the activation of non-basal slips<sup>[24]</sup>, as shown in Fig.4b.

The distributions of the low-angle grain boundaries (LAGBs:  $2^\circ \leq \theta \leq 15^\circ$ ) and high-angle grain boundaries (HAGBs:  $\theta > 15^\circ$ ) are shown in Fig. 5a, where green lines represent LAGBs and black lines represent HAGBs. The extruded MYCNZ alloy exhibits a similar distribution of grain boundaries to the extruded MYC alloy, showing a minor proportion of LAGBs (8.6%) and a significant proportion of HAGBs (91.4%). The presence of these LAGBs, on the one hand, impedes the dislocation movement to enhance the yield strength of the alloy; on the other hand, it facilitates the deformation coordination and mitigates stress concentration near the second phases within  $\alpha$ -Mg matrix to delay the fracture initiation. In contrast, the presence of HAGBs represents the extent of DRX. However, LAGBs can effectively absorb dislocations and subsequently be transformed into HAGBs during the extrusion process, thereby promoting DRX. The volume fraction of DRXed grains increases as the transformation from LAGBs to HAGBs occurs, resulting in a concomitant reduction in grain size<sup>[25]</sup>. Simultaneously, a great number of dislocations form

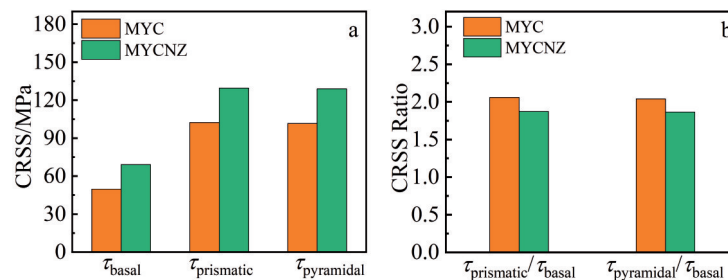


Fig.4 Comparison of CRSS (a) and CRSS ratio (b) of different slip systems in extruded MYC and MYCNZ alloys

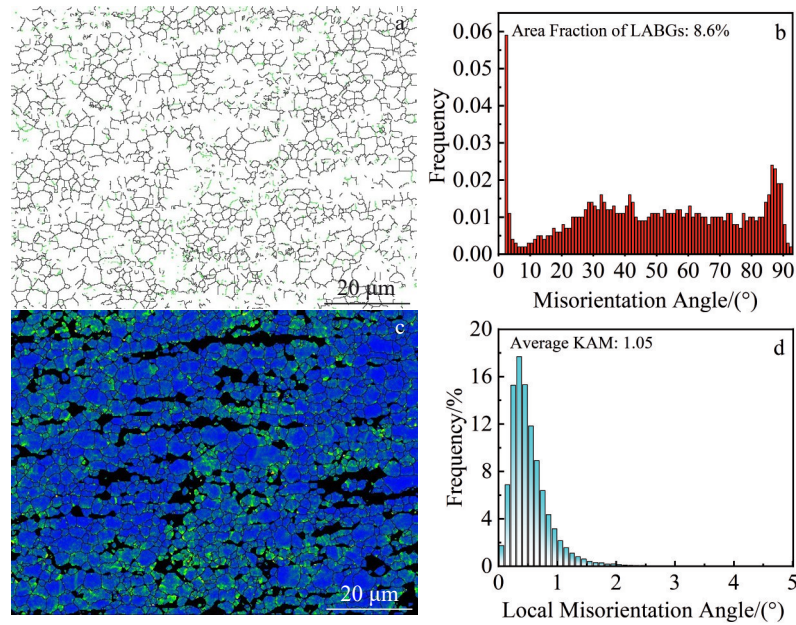


Fig.5 Misorientation angle distribution (a), proportion of LAGBs and HAGBs (b), KAM map (c), and local misorientation angle distribution (d) of extruded MYCNZ alloy

within the deformed grains during the hot extrusion process. The kernel average misorientation (KAM) value is commonly used to estimate the geometrically necessary dislocations (GNDs) in alloys. Fig. 5c shows KAM map of the extruded MYCNZ alloy. GND is accumulated within plastic strain gradient fields and it is considered as an indispensable factor for accommodating the local lattice strains. GND density ( $\rho^{\text{GND}}$ ) can be calculated through Eq.(1)<sup>[26]</sup>, as follows:

$$\rho^{\text{GND}} = \frac{2\Delta\theta_i}{\mu b} \quad (1)$$

where  $\Delta\theta_i$  represents KAM value in radian,  $\mu$  represents the step size of EBSD test (0.2  $\mu\text{m}$  for the extruded MYCNZ alloy), and  $b$  denotes the value of Burgers vector of Mg ( $3.21 \times 10^{-10} \text{ m}^{-2}$ ). Consequently, the  $\rho^{\text{GND}}$  value of the extruded MYCNZ alloy is  $5.71 \times 10^{14} \text{ m}^{-2}$ . This is mainly due to the LPSO and  $\text{Mg}_2(\text{Cu}, \text{Ni}, \text{Zn})$  phases distributed along ED, which effectively hinder the grain boundary mobility during the hot extrusion process, resulting in dislocation accumulation<sup>[27]</sup>.

Fig. 6 reveals the crystal structure and distribution of the precipitated phases in the extruded MYCNZ alloy. As shown in Fig. 6d, the lamellar phase has a lattice spacing of 4.7 nm along the  $c$ -axis, which is around 18 times larger than the lattice spacing of the  $\alpha$ -Mg matrix (0.26 nm). As shown in Fig. 6g, the corresponding SAED pattern shows five weakly diffracted spots between the reflections of  $(0001)_{\text{Mg}}$  and  $(0002)_{\text{Mg}}$ . This observation demonstrates that the lamellar phase is the 18R-LPSO phase<sup>[10]</sup>. Similarly, because the thin striped phase combined has lattice spacing of 3.63 nm along the  $c$ -axis in Fig. 6e and has 13 faint diffraction spots between reflections of  $(0001)_{\text{Mg}}$  and  $(0002)_{\text{Mg}}$  in Fig. 6h, this phase is identified as the 14H-LPSO phase<sup>[28-29]</sup>. The granular phase exhibits an interplanar spacing of 0.474 nm, as shown in

Fig. 6f, which is similar to the  $\text{Mg}_2\text{Cu}$  phase in MYC alloy<sup>[18]</sup>. Based on XRD results (Fig. 2) and SAED pattern in Fig. 6i, it can be inferred that the granular phase corresponds to  $\text{Mg}_2(\text{Cu}, \text{Ni}, \text{Zn})$  phase, exhibiting a tetragonal structure within the  $Fddd$  orthorhombic system with a lattice parameter of  $a=0.28 \mu\text{m}$ .

To understand the types and distribution of dislocations in the extruded alloy, Fig. 7 shows the bright-field and dark-field TEM images of the dislocation distribution within the  $\alpha$ -Mg matrix of the extruded MYCNZ alloy. The phenomenon of numerous observed dislocations is consistent with the calculated dislocation densities from EBSD results. The corresponding variations of dislocation types with  $\mathbf{g}$  and  $\mathbf{b}$  vectors, are listed in Table 1. Combined with the data in Table 1, based on the  $\mathbf{g} \cdot \mathbf{b}$  vector rule, as  $\mathbf{g}=[0002]$ , only  $\langle c+a \rangle$  slips are visible. At  $\mathbf{g}=[10\bar{1}0]$  and  $\mathbf{b}=1/3[\bar{2}110]$  and  $1/3[11\bar{2}0]$ , the  $\langle a \rangle$  slips are visible. At  $\mathbf{g}=[10\bar{1}0]$  and  $\mathbf{b}=1/3[\bar{1}2\bar{1}3]$  and  $1/3[\bar{1}2\bar{1}\bar{3}]$ ,  $\langle c+a \rangle$  slips are invisible. When  $\mathbf{g}=[10\bar{1}1]$  and  $\mathbf{b}=1/3[\bar{1}2\bar{1}0]$ , the  $\langle a \rangle$  slips are invisible. Meanwhile, with  $\mathbf{g}=[10\bar{1}1]$  and  $\mathbf{b}=1/3[\bar{2}113]$  and  $1/3[11\bar{2}\bar{3}]$ ,  $\langle c+a \rangle$  slips are invisible. The weak-beam dark-field TEM images in Fig. 7d–7f with different  $\mathbf{g}$  vectors indicate the presence of multiple  $\langle c+a \rangle$  dislocations and a significant number of  $\langle a \rangle$  dislocations in the extruded MYCNZ alloy. Thus, the co-addition of Ni and Zn can easily result in more non-basal dislocation slips, which can coordinate the  $c$ -axis strain. Additionally, the activated  $\langle c+a \rangle$  dislocations play a crucial role in the plastic deformation of alloys.

### 3.2 Mechanical properties

Fig. 8a presents the hardness values of both extruded alloys. The extruded MYCNZ alloy exhibits a higher hardness (72.7 HV) compared with the extruded MYC alloy (57.7 HV), which is primarily attributed to dispersion strengthening from

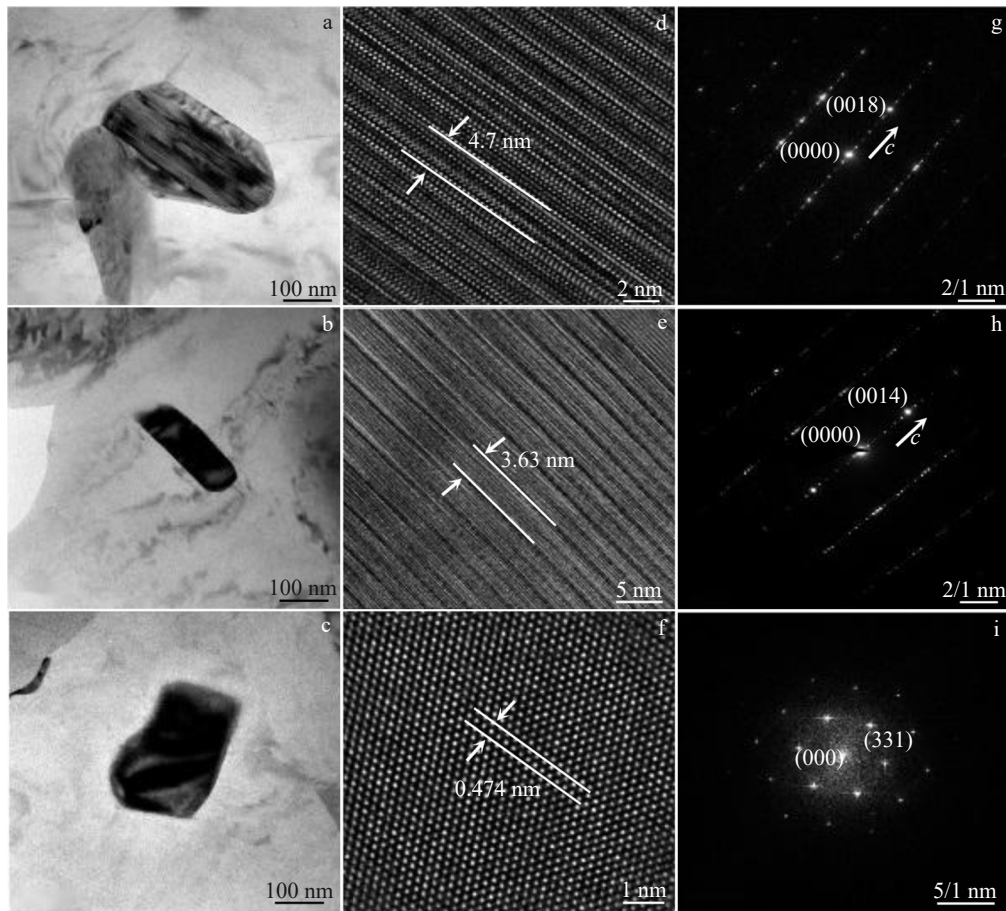


Fig.6 Bright-field TEM images (a–c), HRTEM images (d–f), and corresponding SAED patterns (g–i) of 18R-LPSO phase (a, d, g), 14H-LPSO phase (b, e, h), and  $Mg_2(Cu, Ni, Zn)$  phase (c, g, i)

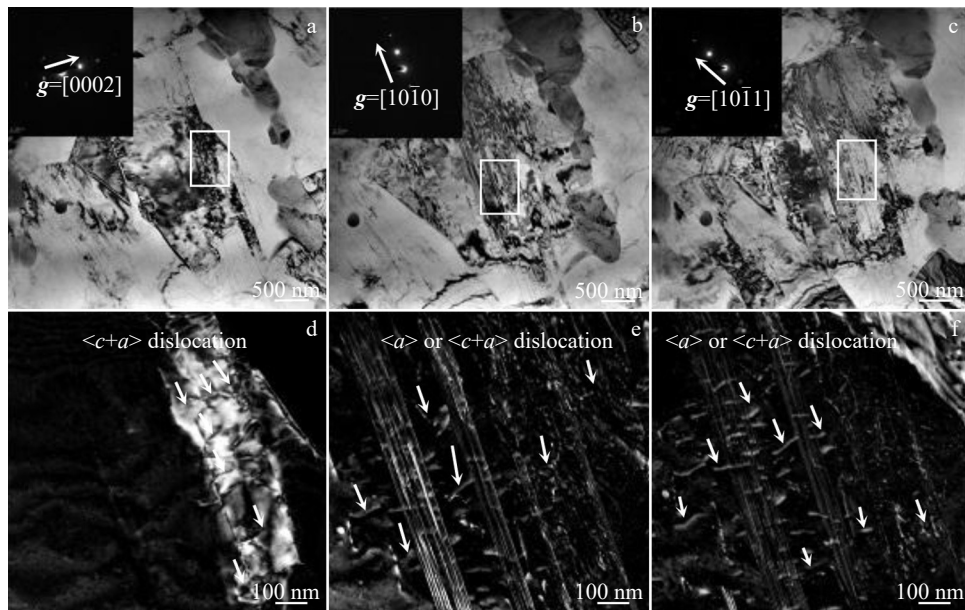


Fig.7 Bright-field (a–c) and dark-field (d–f) TEM images of dislocation distributions and types of extruded MYCNZ alloy: (a, d)  $g=[0002]$ , (b, e)  $g=[10\bar{1}0]$ , and (c, f)  $g=[10\bar{1}1]$

a higher volume fraction of square granular phases and grain boundary strengthening<sup>[30]</sup>. Fig. 8b depicts the engineering stress-engineering strain curves of the extruded alloys at RT

with strain rate of  $1 \times 10^{-3} \text{ s}^{-1}$ . The corresponding mechanical properties of extruded MYC and MYCNZ alloys are listed in Table 2. At RT, the extruded MYCNZ alloy demonstrates

**Table 1** Variation of dislocation types with diffraction vectors and Burgers vectors for extruded MYCNZ alloy

$g$	$b/\times 1/3$										
	$\langle a \rangle$					$\langle c+a \rangle$					$\langle c \rangle$
	$\pm[110]$	$\pm[\bar{1}2\bar{1}0]$	$\pm[\bar{2}110]$	$\pm[11\bar{2}3]$	$\pm[\bar{1}2\bar{1}3]$	$\pm[\bar{2}113]$	$\pm[11\bar{2}\bar{3}]$	$\pm[\bar{1}2\bar{1}\bar{3}]$	$\pm[\bar{2}11\bar{3}]$	$\pm[0003]$	
[0002]	0	0	0	$\pm 2$	$\pm 2$	$\pm 2$	2	2	2	$\pm 2$	
[10 $\bar{1}0$ ]	$\pm 1$	0	$\pm 1$	$\pm 1$	0	$\pm 1$	$\pm 1$	0	$\pm 1$	0	
[10 $\bar{1}1$ ]	$\pm 1$	0	$\pm 1$	$\pm 2$	$\pm 1$	0	0	$\pm 1$	$\pm 2$	$\pm 1$	

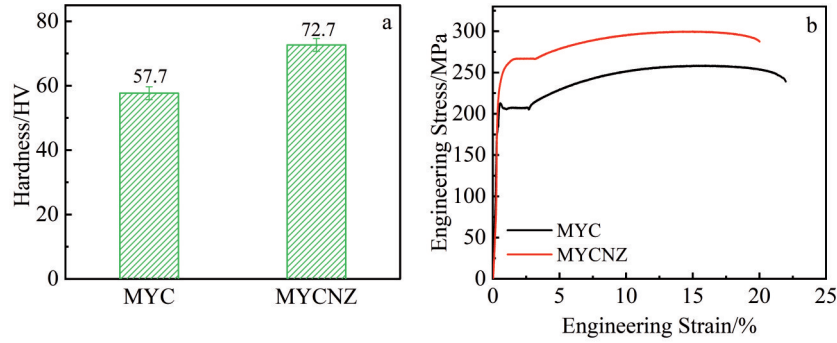


Fig.8 Hardness (a) and engineering stress-engineering strain curves (b) of extruded MYC and MYCNZ alloys

**Table 2** Mechanical properties of extruded MYC and MYCNZ alloys at RT

Extruded alloy	$\sigma_b$ /MPa	$\sigma_{0.2}$ /MPa	$\varepsilon_L$ /%	Hardness/HV
MYC	257.8	207.3	22.0	57.7
MYCNZ	299.8	266.9	20.1	72.7

yield strength ( $\sigma_{0.2}$ ) of 266.9 MPa, ultimate tensile strength ( $\sigma_b$ ) of 299.8 MPa, and elongation to fracture ( $\varepsilon_L$ ) of 20.1%. Compared with those of the extruded MYC alloy,  $\sigma_{0.2}$  and  $\sigma_b$  values of the extruded MYCNZ alloy increase by 28.7% and 16.3%, respectively. Besides, the extruded MYC and MYCNZ alloys show excellent elongation to fracture ( $\varepsilon_L$ ) values of 22.0% and 20.1%, respectively. In addition, the extruded MYCNZ alloy exhibits a higher  $\sigma_{UTS} \times \varepsilon_L$  value (6.03 GPa·%) than the extruded MYC alloy (5.67 GPa·%)<sup>[18]</sup>. Therefore, the above experimental results indicate that the alloy demonstrates a high strength-ductility synergy by the co-addition of Ni and Zn. Fig. 9 displays the tensile fracture morphologies of the extruded MYC and MYCNZ alloys. Fig.9a exhibits an obvious necking phenomenon in the tensile samples of both extruded alloys after fracture, indicating the ductile fracture behavior. As shown in Fig. 9b and 9f, the extension direction of microcracks in two extruded alloys is almost perpendicular to the direction of stretching, which thereby proves that the normal stress leads to the nucleation and propagation of microcracks<sup>[31]</sup>. As shown in Fig.9c and 9g, a significant number of microcracks are observed surrounding certain particles and LPSO phases. Meanwhile, a multitude of slip lines appear near the microcracks with kinking phenomena, which indicates the non-basal slips. Thus, good ductility of both extruded alloys is caused by the substantial activation of the non-basal slips. Moreover, the presence of numerous dimples on the fracture surfaces also further

confirms that these two extruded alloys have good ductility<sup>[32]</sup>.

### 3.3 Effects of co-addition of Ni and Zn on tensile yield strength of Mg-Y-Cu alloy

The enhancement in mechanical properties of the extruded MYCNZ alloy primarily arises from grain boundary strengthening, dislocation strengthening, and second phase strengthening. To quantify the role of various strengthening mechanisms on the tensile yield strength of extruded alloys, the contributing values of these primary strengthening mechanisms are calculated<sup>[33]</sup>, as follows:

$$\sigma_{YS} = \sigma_{GB} + \sigma_{loca} + \sigma_{sec} \quad (2)$$

where  $\sigma_{YS}$ ,  $\sigma_{GB}$ ,  $\sigma_{loca}$ , and  $\sigma_{sec}$  indicate the contributing value of yield strength, grain boundary strengthening, dislocation strengthening, and second phase strengthening, respectively.

Firstly, the contribution of grain boundary strengthening to the yield strength of extruded alloys can be calculated using the Hall-Petch formula<sup>[34]</sup>, as follows:

$$\sigma_{GB} = \sigma_0 + kd^{-1/2} \quad (3)$$

where  $\sigma_0$  is the frictional stress,  $d$  is the average grain size, and  $k$  is a fixed stress concentration factor. In this case,  $\sigma_0=16$  MPa and  $k=220$  MPa· $\mu\text{m}^{-1/2}$  for Mg-Y alloy<sup>[34]</sup>. In this research, the average grain size of the extruded MYCNZ alloy is 2.62  $\mu\text{m}$ . Therefore, the calculated value for the extruded MYCNZ alloy is 151.9 MPa. Secondly, the contribution to strengthening from residual dislocations<sup>[35]</sup> can be evaluated, as follows:

$$\sigma_{loca} = \alpha Gb\sqrt{\rho} \quad (4)$$

where  $\alpha$  represents a constant value of 0.2,  $G$  denotes the shear modulus (approximately 17 GPa),  $b$  is the value of Burgers vector ( $|b|=0.32$  nm), and  $\rho$  represents the dislocation density of the extruded alloy. Based on the preceding calculation, the  $\rho^{\text{GND}}$  of the extruded MYCNZ alloy is determined as  $5.71 \times 10^{14} \text{ m}^{-2}$ . The calculated value for the

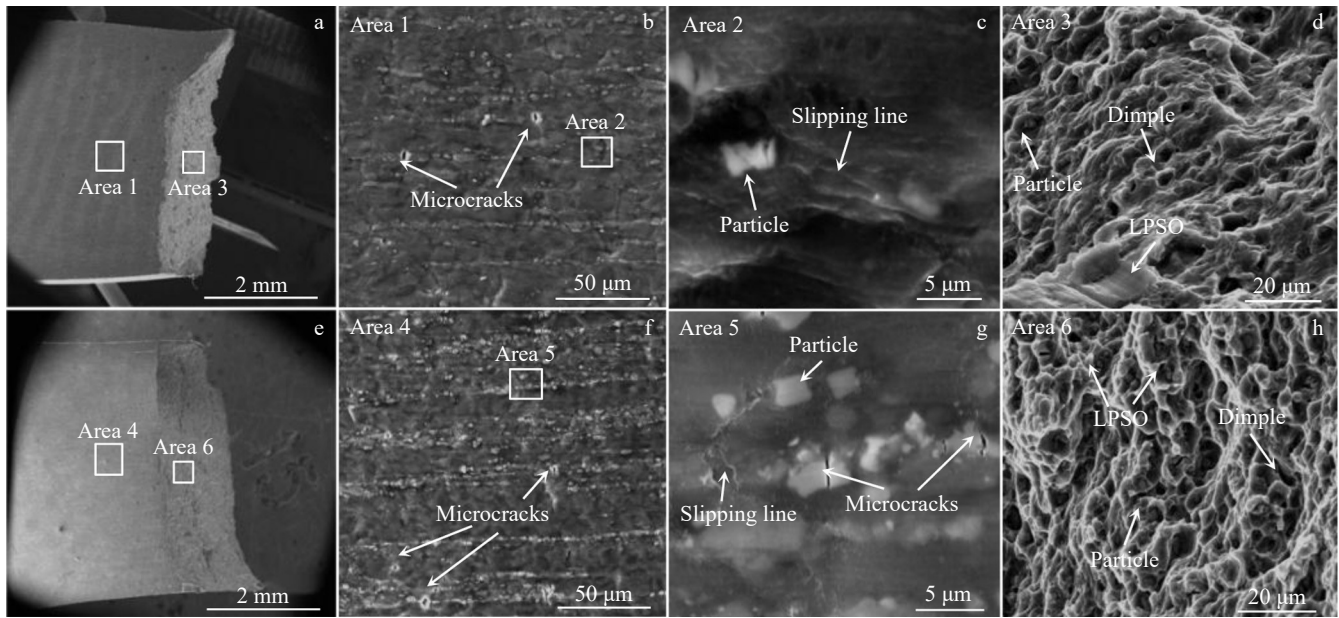


Fig.9 Tensile fracture morphologies of extruded MYC alloy (a-d) and MYCNZ alloy (e-h)

extruded MYCNZ alloy is approximately 26 MPa. Thirdly, the second phase can be further classified into the lamellar 18R-LPSO phase, blocky 18R-LPSO phase, granular  $Mg_2(Cu, Ni, Zn)$  phase, and thin striped 14H-LPSO phase. Among these particles, the lamellar 18R-LPSO phase serves as a strengthening phase due to its exceptional hardness and elastic modulus. This phase effectively undergoes load transfer from the soft  $\alpha$ -Mg matrix, allowing the extruded alloy to withstand higher stresses. Thus, the contribution of the lamellar phase to yield strength can be determined by the load transfer formula<sup>[36]</sup>, as follows:

$$\Delta\sigma_{L-18R} = V_f\sigma_f + \sigma_m(1 - V_f) \quad (5)$$

$$\sigma_m = K_s1C_Y^n + K_s2C_{Zn}^n + K_s3C_{Co}^n + K_s4C_{Zn}^n + \sigma_{Mg} \quad (6)$$

$$K_s = (38.9 \text{ MPa}) \times \left[ \left( \frac{\varepsilon_b}{0.176} \right)^2 + \left( \frac{\varepsilon_{SFE}}{5.67} \right)^2 - \frac{\varepsilon_b \varepsilon_{SFE}}{2.98} \right]^{4/3} \quad (7)$$

where  $V_f$  represents the volume fraction of the 18R-LPSO lamellar phase;  $\sigma_f$  and  $\sigma_m$  are the yield strengths of the LPSO phase and  $\alpha$ -Mg solid solution, respectively, with  $\sigma_m=70$  MPa and  $\sigma_f=205$  MPa;  $n$  is the locking parameter of 1/2;  $K_s$  is functions and modulus differences concerning atomic size mismatch between solute and matrix;  $C_s$  denotes the concentration of the solute atoms;  $\varepsilon_b$  stands for the size mismatch;  $\varepsilon_{SFE}$  refers to the chemical mismatch. In the extruded MYCNZ alloy, the volume fraction of the lamellar 18R-LPSO phase is 11.6%, contributing to yield strength by 21.8 MPa. Additionally, the blocky 18R-LPSO phase and granular  $Mg_2(Cu, Ni, Zn)$  phase with average size below 1  $\mu m$  can effectively impede dislocation movement. Thus, the granular  $Mg_2(Cu, Ni, Zn)$  phase and blocky 18R-LPSO phase exhibit significant resistance to the dispersion strengthening<sup>[37]</sup>, as expressed by Eq.(8), as follows:

$$\Delta\sigma_p = 4\phi\gamma G_m V \varepsilon \quad (8)$$

where  $\gamma$  is a factor associated with the Poisson's ratio with  $\gamma=1/[2(1-\nu)]$ ,  $\nu=0.35$ , and  $\phi=G^*/[G^*-\gamma(G^*-G_m)]$ ;  $G_m$  represents

the shear modulus of the  $\alpha$ -Mg matrix value (16.6 GPa);  $G^*$  is the shear modulus of the 18R-LPSO phase (21.5 GPa)<sup>[38]</sup>;  $V$  denotes the volume fraction of the blocky 18R-LPSO phases and granular phases  $Mg_2(Cu, Ni, Zn)$ ;  $\varepsilon$  stands for the uniform plastic strain ( $\varepsilon=0.01$ ). The volume fractions of the blocky 18R-LPSO phases and granular  $Mg_2(Cu, Ni, Zn)$  phases are 2.6% and 6.4%, respectively. Thus, the enhancement value in yield strength by the granular  $Mg_2(Cu, Ni, Zn)$  phases and the blocky 18R-LPSO phases are 45.2 and 16.1 MPa, respectively. The thin striped 14H-LPSO phases and stacking faults in the  $\alpha$ -Mg matrix can be regarded as the strengthening phase of the extruded MYCNZ alloy. During deformation, these phases increase the yield strength of the extruded alloy by hindering dislocation movement, and their contributions can be quantified using the Orowan strengthening mechanism<sup>[24]</sup>, as follows:

$$\Delta\sigma_{Orowan} = \frac{G_m b}{2\pi\lambda \sqrt{(1-\nu)}} \ln \left( \frac{d_p}{b} \right) \quad (9)$$

where  $G_m$  represents the shear modulus of the  $\alpha$ -Mg matrix with the value of 16.6 GPa,  $b$  denotes the value of Burgers vector as 0.32 nm,  $\nu$  is the Poisson's ratio as 0.35, and  $d_p$  represents the average diameter of the thin striped 14H-LPSO phase and stacking faults. The results are listed in Table 3. Additionally,  $\lambda$  is the measured average particle spacing, which can be expressed by Eq.(10), as follows:

$$\lambda = 0.825 \sqrt{\frac{l_p t_p}{V_p}} - 0.393 l_p - 0.866 t_p \quad (10)$$

where  $l_p$  is the average length,  $t_p$  is the average width, and  $V_p$  is volume fraction of the thin striped 14H-LPSO phase and stacking faults. The corresponding calculation results are presented in Table 3. Thus, the yield strength caused by the Orowan mechanism of the extruded MYCNZ alloy is 11.4 MPa. Fig.10 and Table 3 show the contribution from various

**Table 3** Various strengthening mechanisms and corresponding microstructure parameters of extruded MYCNZ alloy

Alloy	$d_G/\mu\text{m}$	$\sigma_{GB}/\text{MPa}$	$\rho^{\text{GND}}/\text{m}^{-2}$	$\Delta\sigma_{\text{loca}}/\text{MPa}$	$V_{\text{B-18R}}/\%$	$V_{\text{Mg}_2(\text{Cu, Ni, Zn})}/\%$	$\Delta\sigma_p/\text{MPa}$	$V_{\text{L-18R}}/\%$	$\Delta\sigma_L/\text{MPa}$	$V_{\text{14H+SFs}}/\%$	$d_{\text{14H+SFs}}/\mu\text{m}$	$\lambda_{\text{14H+SFs}}/\mu\text{m}$	$\Delta\sigma_{\text{Orowan}}/\text{MPa}$
MYCNZ	2.62	151.9	$5.71 \times 10^{14}$	26	2.6	6.4	61.3	11.6	21.8	5.1	0.27	0.66	11.4

Note:  $d_G$  is mean grain size;  $\sigma_{GB}$  is the increment in yield strength due to grain refinement;  $\rho^{\text{GND}}$  is GND density;  $\Delta\sigma_{\text{loca}}$  is yield strength increment in load-bearing strengthening;  $V_{\text{B-18R}}$  is the volume fraction of blocky phase;  $V_{\text{Mg}_2(\text{Cu, Ni, Zn})}$  is the volume fraction of particle phase;  $\Delta\sigma_L$  is the yield strength increment in lamellar phase;  $\Delta\sigma_p$  is the yield strength increment in dispersion strengthening;  $V_{\text{L-18R}}$  is the volume fraction of lamellar 18R-LPSO phase;  $d_{\text{14H+SFs}}$  is the mean particle size;  $\lambda_{\text{14H+SFs}}$  is interparticle distance;  $V_{\text{14H+SFs}}$  is the volume fraction of 14H-LPSO phase and SFs;  $\Delta\sigma_{\text{Orowan}}$  is the yield strength increment caused by particle strengthening.

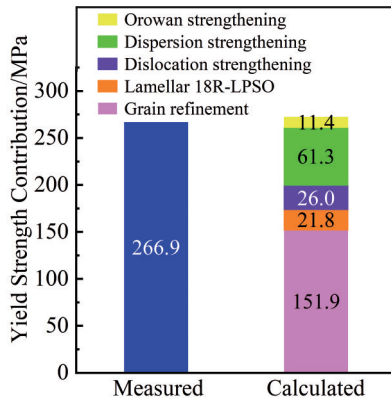


Fig. 10 Yield strength contributed by different strengthening mechanisms of extruded MYCNZ alloy

strengthening mechanisms to yield strength of the extruded MYCNZ alloy. Among these strengthening mechanisms, grain refinement is the primary factor to enhance yield strength, followed by LPSO phase strengthening.

### 3.4 Effects of co-addition of Ni and Zn on ductility of Mg-Y-Cu alloy

The co-addition of Ni and Zn not only enhances the tensile strength, but also retains the ductility of the extruded MYC alloy. Firstly, the co-addition of Ni and Zn results in an obvious random texture, weakening the basal texture of the extruded MYCNZ alloy (Fig. 3). The presence of numerous DRX grains in the extruded alloy is responsible for the weakened texture intensity, effectively enhancing the ductility of the extruded alloy<sup>[11]</sup>. Secondly, the grain size of the extruded MYCNZ alloy is significantly refined to 2.62  $\mu\text{m}$  after the co-addition of Ni and Zn. This is mainly due to DRX behavior of dispersed submicron particles through the particle-stimulated nucleation mechanism<sup>[39]</sup>. These fine DRX grains, on the one hand, can reduce the dislocation pileup within the individual grains, leading to uniform distribution of the deformation of alloy; on the other hand, they can facilitate the grain rotation and the grain boundary sliding, thereby suppressing the formation of microcracks<sup>[7]</sup>. Moreover, this grain refinement also prevents the transition from  $\langle c+a \rangle$  dislocations to immovable  $\langle c+a \rangle$  or  $\langle c \rangle$  dislocations, ultimately enhancing the ductility of Mg alloys<sup>[40]</sup>. Thirdly, a significant quantity of  $\langle a \rangle$  and  $\langle c+a \rangle$  dislocations appear in the  $\alpha$ -Mg matrix of the extruded MYCNZ alloy (Fig. 7). This phenomenon is beneficial to the ductility of Mg-based alloys as it accommodates  $c$ -axis strain and satisfies the Von-Mises

deformation criterion<sup>[41]</sup>. Meanwhile, the slip resistance between the basal and non-basal slip systems is effectively reduced, which is beneficial to the initiation of the non-basal slips and enhances the ductility of Mg-based alloys<sup>[42]</sup>. The lower  $\tau_{\text{prism}}/\tau_{\text{basal}}$  and  $\tau_{\langle c+a \rangle}/\tau_{\text{basal}}$  values of both extruded alloys (Fig. 4) suggest that the non-basal slips are easily activated, thereby promoting more homogeneous plastic deformation of the grains and reducing the stress concentration<sup>[43]</sup>. Finally, it can be seen that the presence of the kink bands of LPSO phase can alter the stress concentration during deformation, ultimately enhancing ductility<sup>[44]</sup>. Therefore, the aforementioned size, orientation, and distribution of grains are closely associated with the high ductility in the extruded MYCNZ alloy.

## 4 Conclusions

1) The as-cast MYCNZ alloy consists of 18R-LPSO phase,  $\text{Mg}_2(\text{Cu, Ni, Zn})$  phase, and a smaller amount of MgY and Y-rich phase. After homogenization, the alloy undergoes a phase transition from the 18R-LPSO phase to the 14H-LPSO phase. Compared with the homogenized MYC alloy, the volume fraction of LPSO phases in MYCNZ alloy decreases, whereas that of the granular phase shows a significant increase of 58.4%.

2) After extrusion, the grains of the homogenized MYC and MYCNZ alloys are significantly refined and the average grain sizes are approximately 3.69 and 2.62  $\mu\text{m}$ , respectively. The extruded MYCNZ alloy shows a weaker basal texture with texture intensity of 4.05, compared with the extruded MYC alloy. Additionally, the non-basal slips can be observed in the extruded MYCNZ alloy, including  $\langle a \rangle$  and  $\langle c+a \rangle$  dislocations.

3) The extruded MYCNZ alloy has higher  $\sigma_{0.2}$  and  $\sigma_b$ , whose values are 266.9 and 299.8 MPa, increasing by 28.7% and 16.3%, respectively, compared with those of the extruded MYC alloy. This result indicates that the extruded MYCNZ alloy exhibits a better synergy effect of strength and ductility ( $\sigma_{\text{UTS}} \times \varepsilon_L = 6.03 \text{ GPa}\cdot\%$ ), compared with that of the extruded MYC alloy (5.67  $\text{GPa}\cdot\%$ ). The excellent combined mechanical properties of the extruded MYCNZ alloy are mainly attributed to grain refinement, LPSO phase strengthening, weakening texture, and the activation of non-basal slips.

## References

- 1 Prasad S V S, Prasad S B, Verma K et al. *Journal of Magnesium*

- and Alloys[J], 2022, 10(1): 1
- 2 Yang Y, Xiong X M, Chen J et al. *Journal of Magnesium and Alloys*[J], 2023, 11(8): 2611
- 3 Liu B, Yang J, Zhang X Y et al. *Journal of Magnesium and Alloys*[J], 2023, 11(1): 15
- 4 Wu G, Wang C L, Sun M et al. *Journal of Magnesium and Alloys*[J], 2021, 9(1): 1
- 5 Song J F, She J, Chen D L et al. *Journal of Magnesium and Alloys*[J], 2020, 8(1): 1
- 6 Gong Yuan, He Jinguang, Wen Jiuba et al. *Rare Metal Materials and Engineering*[J], 2023, 52(2): 508 (in Chinese)
- 7 Zhang Z, Zhang J H, Wang J et al. *International Journal of Minerals, Metallurgy and Materials*[J], 2020, 28(1): 30
- 8 Shi B Q, Chen R S, Ke W. *Journal of Alloys and Compounds*[J], 2011, 509(7): 3357
- 9 Liu H, Huang H, Sun J P et al. *Acta Metallurgica Sinica (English Letters)*[J], 2018, 32(3): 269
- 10 Bi G L, Wang Y S, Jiang J et al. *Journal of Alloys and Compounds*[J], 2021, 881: 160577
- 11 Jin Z Z, Zha M, Wang S Q et al. *Journal of Magnesium and Alloys*[J], 2022, 10(5): 1191
- 12 Ding Z B, Zhao Y H, Lu R P et al. *Transactions of Nonferrous Metals Society of China*[J], 2019, 29(4): 722
- 13 Liu K, Zhang J H, Sun W et al. *Journal of Materials Science*[J], 2009, 44(1): 74
- 14 Bi G L, Man H S, Jiang J et al. *Journal of Materials Research and Technology*[J], 2022, 20: 590
- 15 Wu S Z, Qiao X G, Qin S H et al. *Materials Science and Engineering A*[J], 2022, 831: 142198
- 16 Zhang S R, Kim J, Wang F X et al. *Materials Characterization*[J], 2022, 191: 112111
- 17 Zhou X J, Liu C M, Gao Y H et al. *Journal of Alloys and Compounds*[J], 2018, 749: 878
- 18 Bi G L, Zhang N M, Jiang J et al. *Journal of Rare Earths*[J], 2023, 41(3): 454
- 19 Jin Q Q, Shao X H, Hu X B et al. *Philosophical Magazine*[J], 2016, 97(1): 1
- 20 Zhu Y M, Morton A J, Nie J F. *Acta Materialia*[J], 2010, 58(8): 2936
- 21 Wang H M, Wu P D, Kurukuri S et al. *International Journal of Plasticity*[J], 2018, 107: 207
- 22 Zeng Y, Shi O L, Jiang B et al. *Journal of Alloys and Compounds*[J], 2018, 764: 555
- 23 Pan H C, Xie D, Li J R, et al. *Materials Research Letters*[J], 2021, 9(8): 329
- 24 Wan Y J, Zeng Y, Dou Y C et al. *Journal of Magnesium and Alloys*[J], 2022, 10(5): 1256
- 25 Pan H C, Kang R, Li J R et al. *Acta Materialia*[J], 2020, 186: 278
- 26 Zhang K, Shao Z T, Daniel C S et al. *Materials Science and Engineering A*[J], 2021, 807: 140821
- 27 Xie J S, Zhang Z, Liu S J et al. *International Journal of Minerals, Metallurgy and Materials*[J], 2022, 30(1): 82
- 28 Hao J Q, Zhang J S, Li B Q et al. *Materials Science and Engineering A*[J], 2021, 804: 140727
- 29 Pan H C, Huang Q Y, Qin G W et al. *Journal of Alloys and Compounds*[J], 2017, 692: 898
- 30 Bi G L, Han Y X, Jiang J et al. *Materials Science and Engineering A*[J], 2019, 760: 246
- 31 Bi G L, Han Y X, Jiang J et al. *Rare Metals*[J], 2018, 38(8): 739
- 32 Liu J A, Wang J L, Yang M L et al. *Metals and Materials International*[J], 2020, 27(6): 1613
- 33 Hansen N. *Scripta Materialia*[J], 2004, 51(8): 801
- 34 Wen Y, Guan B, Xin Y C et al. *Scripta Materialia*[J], 2022, 210: 114451
- 35 Wang S C, Zhu Z, Starink M J. *Journal of Microscopy*[J], 2005, 217: 174
- 36 Shi B Q, Chen R S, Ke W. *Journal of Alloys and Compounds*[J], 2011, 509(7): 3357
- 37 Cáceres C H, Davidson C J, Griffiths J R et al. *Materials Science and Engineering A*[J], 2002, 325(1): 344
- 38 Tane M, Nagai Y, Kimizuka H et al. *Acta Materialia*[J], 2013, 61(17): 6338
- 39 Duan M, Luo L, Liu Y. *Journal of Alloys and Compounds*[J], 2020, 823: 153691
- 40 Wu Z X, Curtin W A. *Nature*[J], 2015, 526(7571): 62
- 41 Agnew S R, Duygulu Ö. *International Journal of Plasticity*[J], 2005, 21(6): 1161
- 42 Shao X H, Yang Z Q, Ma X L. *Acta Materialia*[J], 2010, 58(14): 4760
- 43 Zhou S B, Liu T T, Tang A T et al. *Materials and Design*[J], 2023, 225: 111476
- 44 Egusa D, Yamasaki M, Kawamura Y et al. *Materials Transactions*[J], 2013, 54(5): 698

## Ni和Zn复合添加对挤压态Mg-Y-Cu合金显微组织和力学性能的影响

毕广利<sup>1,2</sup>, 魏智超<sup>1,2</sup>, 姜静<sup>1,2</sup>, 张妞明<sup>3</sup>, 李元东<sup>1,2</sup>, 陈体军<sup>1,2</sup>

(1. 兰州理工大学 省部共建有色金属先进加工与再利用国家重点实验室, 甘肃 兰州 730050)

(2. 兰州理工大学 材料科学与工程学院, 甘肃 兰州 730050)

(3. 贵州航天风华精密设备有限公司, 贵州 贵阳 550000)

**摘要:** 研究了Ni和Zn复合添加对挤压态Mg-6.84Y-2.45Cu (MYC, 质量分数)合金显微组织和力学性能的影响。结果表明: 铸态Mg-6.79Y-1.21Cu-1.12Ni-1.25Zn (MYCNZ, 质量分数)合金组织由 $\alpha$ -Mg、层片状18R-长周期堆垛有序(LPSO)相、 $Mg_2$ (Cu, Ni, Zn)颗粒相以及少量的富Y相组成。均匀化处理后, MYCNZ合金发生了相变, 部分晶界处片层状的18R-LPSO相转变为晶内细针状的14H-LPSO相。挤压后, 合金第二相的数量、形态和分布都发生了改变, 同时晶粒尺寸显著细化至2.62  $\mu\text{m}$ , 该合金也形成了较弱的基面织构。拉伸试验结果表明, Ni和Zn的复合添加显著提高了挤压态MYC合金的抗拉伸强度, 同时保持了良好的塑性。挤压态MYCNZ合金的屈服强度、极限抗拉伸强度和断裂伸长率分别为266.9 MPa、299.8 MPa和20.1%。该合金具有良好的强塑性协同效应。挤压态MYCNZ合金在室温下的高抗拉伸强度主要是由于晶粒细化和第二相强化, 而良好的塑性主要是源于织构弱化和非基面位错的激活。

**关键词:** 挤压Mg-Y-Cu(Ni, Zn)合金; LPSO相; 显微组织; 力学性能

**作者简介:** 毕广利, 男, 1981年生, 博士, 教授, 兰州理工大学省部共建有色金属先进加工与再利用国家重点实验室, 甘肃 兰州 730050, 电话: 0931-2976378, E-mail: glbi@163.com